Article

Numerical Simulation of Gas Production Behavior Using Radial Lateral Well and Horizontal Snake Well Depressurization Mining of Hydrate Reservoir in the Shenhu Sea Area of the South China Sea

Tinghui Wan [1,2], Mingming Wen [1,2,*], Hongfeng Lu [1,2], Zhanzhao Li [1,2], Zongheng Chen [1,2], Lieyu Tian [1,2], Qi Li [1,2], Jia Qu [1,2] and Jingli Wang [1,2,*]

1 Guangzhou Marine Geology Survey, China Geological Survey, Ministry of Natural Resources, Guangzhou 511458, China; atomion@126.com (T.W.); gmgslhf@126.com (H.L.); 13650780173@163.com (Z.L.); czhgs@126.com (Z.C.); tianlieyu23@163.com (L.T.); liqi3412@163.com (Q.L.); qujia2261520@163.com (J.Q.)
2 National Engineering Research Center for Gas Hydrate Exploration and Development, Guangzhou 511458, China
* Correspondence: wmingming@mail.cgs.gov.cn (M.W.); wjl06012527@126.com (J.W.)

Abstract: Improving the production capacity of natural gas hydrates (NGHs) is crucial for their commercial development. Based on the data of the first on-site testing production of NGHs in the Shenhu Sea area, numerical methods were used to analyze the production behavior of radial lateral well (RLW) and horizontal snake well (HSW) with different completion lengths when they deployed at different layers of the Class-1 type hydrate reservoir (with a fixed pressure difference of 6 MPa and continuous production for 360 days). The results indicate that compared with the single vertical well production, RLW and HSW can effectively increase production capacity by enlarging drainage area and the productivity is directly proportional to the total completion length. The RLW and HSW deployed at the three-phase layer (TPL) have optimal mining performance within a 360-day production period. Different to the previous research findings, during a short-term production period of 360 days, regardless of the deployment layer, the overall production capacity of HSW is better than RLW's. The total gas production of HSW-2 circles well type is about four times that of a single vertical well, reaching 1.554×10^7 ST m^3. Moreover, the HSW-1 lateral well type stands out with an average Q_g of 3.63×10^4 ST m^3/d and a specific production index J of 16.93; it has the highest J-index among all well types, which means the best mining efficiency. It is recommended to choose the HSW-1 circle well type, if the coiled tubing drilling technique is used for on-site testing production of NGHs in the future. The research results provide insights into the potential applications of RLW and HSW in this sea area.

Keywords: natural gas hydrate; continuous tubing drilling; radial lateral well; horizontal snake well; numerical simulation

1. Introduction

Natural gas hydrates (NGHs) as an unconventional clean energy source are widely distributed and have huge reserves with great potential for commercial development [1–4]. The superiority of the depressurization method has been confirmed by recent offshore NGH testing production activities [5–8]. However, the production capacity of offshore NGH testing conducted by China and Japan is still far below the commercial standard of 50×10^4 m^3/d [1]. Due to the significant gap between the daily production capacity of offshore NGH testing production and the industrialization threshold, achieving low-cost and efficient NGH development becomes a key challenge [9]. After conducting a systematic analysis of the entire NGH development process, Wu et al. believe that the most promising development direction to break through the bottleneck of NGH industrialization is the

composite production mode of complex structured well (such as horizontal wells, radial lateral wells, and fishbone wells, etc.,) or group wells (well network) mainly consisting of multiple vertical/horizontal wells for depressurization mining combined with auxiliary heating (cable heating, microwave heating, and electromagnetic heating, etc.,) whilst simultaneously adopting stimulation techniques that are suitable for the target reservoir, such as CO_2 cap reconstruction, near wellbore reservoir hydraulic jet grouting, hydraulic fracturing, steam or brine injection [9]. Among them, the main approach for stimulation is to construct complex structured wells such as horizontal wells and radial lateral wells, etc., with the main mechanism for stimulation enlarging the drainage area [9]. Ye H et al. observed that a directional well and a multilateral well may significantly boost productivity, particularly in cluster wells, which can increase gas productivity by up to 2.2 times that of a single well [10]. Mao et al. investigated the impact of various helical multilateral well parameters on production capacity and concluded that it has the potential to achieve commercial exploitation of NGHs [11]. Xin X et al. discovered that the depth of laterals in a multilateral well is a critical factor determining production capacity [12]. Ye H et al. investigated the effect of various parameter settings of various well types, and the findings revealed that branch parameters had the greatest influence on the productivity [13]. Hao Y et al. discovered that fishbone wells are the best well types for long-term development of NGHs [14]. Jin G et al. discovered that interference at the multilateral well intersections can increase hydrate dissociation [15]. According to research by He J et al., the single horizontal well's production capacity was only around 59.3% lower than that of the six-branch fishbone well [16]. Cao X et al. discovered that well interference of a multibranch well is adverse to gas production [17]. Previous research has substantially prompted the application of complex structured wells in NGH development.

The coiled tubing drilling technique is widely used in conventional oil and gas extraction, due to its strong technical feasibility and low-cost advantages [18–22]. In recent years, the application of this technique in the mining of NGHs has received increasing attention. The primary research focus is applying the continuous tubing drilling technique to complete the drilling of two types of complex structured wells: horizontal serpentine wells and radial horizontal wells. For example, Wan et al. explored the technical feasibility of using the coiled tubing drilling technique for HSW drilling in NGH reservoirs. The research results verified the feasibility of the technology and the HSW can effectively improve the production capacity, reduce wellbore collapse problems, and has a relatively low cost [23]. Li et al. proposed a new method of using radial jet drilling to extract hydrates provided by the corresponding process flow and studied the extension limit and monitoring of the borehole trajectory [24]. Mahmood et al., using analytical models, investigated the gas production of RLW and HSW in extracting hydrates and found that the production capacity of RLW is positively correlated with the laterals's quantity, length, and radius, while the production capacity of HSW is positively correlated with the length and radius of the wellbore [25]. Zhang et al. found that radial wells can significantly increase production capacity in the early stage of hydrate depressurization mining, and the lateral length is the main controlling factor for overall production capacity [26,27]. Zhang et al.'s experiment simulated the extraction of hydrates in water-rich hydrate samples via vertical and radial wells, and found that the gas and water production of the radial well was approximately 120% and 139% of the vertical well, respectively [28]. Wan et al. conducted a numerical evaluation of the gas production capacity of different radial lateral wellbore deployment schemes in the Shenhu Sea area hydrate reservoir. The results indicate that radial lateral wellbore can effectively improve production efficiency [29]. According to the progress of continuous tubing drilling technology in hydrate development in the past decade (Table 1), it can be seen that there is currently limited research on the RLW and HSW, therefore this work was based on on-site data from China's first offshore NGH testing production and analyzed the gas and water production behavior of RLW and HSW with different completion layers and lateral lengths. The results provide a theoretical reference for the practical application of the above well types in the Shenhu Sea area.

Table 1. Progress of coiled tubing drilling technique in hydrate development.

Author	Year	Input	Work Summary	Output
Cinelli et al. [18]	2013	Technical review	Introduced the equipment and technical process of coiled tubing drilling, using a low permeability oilfield as an example to detail the completion process and production statistics for radial jet drilling.	Coiled tubing drilling technique is a low-cost and environmentally friendly method to improve productivity.
Kamel et al. [19,20]	2016, 2017	Technical review	Introduced the theoretical, and technological progress, procedures, applications, and challenges of coiled tubing drilling technique. Several global case studies were discussed.	Coiled tubing drilling technique is effective for increasing production, and is a feasible and cost-effective alternative to marginal oilfield fracturing.
Huang et al. [22]	2019	Technical review	Introduced the technical characteristics, advantages, and limitations of coiled tubing drilling technique. Discussed the drilling performance and trajectory measurement methods.	Coiled tubing drilling technique is a flexible new geo-energy development technology.
Wan et al. [23]	2019	Analytical model	Explored the feasibility of developing NGHs v HSW. Provided an analytical model to calculate the maximum achievable wellbore length (MAWL). Predict the production capacity based on the Furui equation.	The HSW mining technology is feasible for offshore NGHs, and demonstrates how to evaluate its productivity and economy.
Li et al. [24]	2020	Analytical model, experiment, and numerical simulation	Introduced the process flow of developing NGHs via radial lateral wells, the ability of jet rock breaking drilling, the feeding method and extension limit of jet drill bits, wellbore trajectory measurement, and control.	A new approach was proposed to develop marine NGHs using an integrated method of cavitation jet drilling radial horizontal wells and screen tube completion.
Mahmood et al. [25]	2021	Analytical model	Compared the production potential of HSW and RLW using the developed analytical model and on-site case data of NGH reservoirs in the South China Sea.	RLW produce slightly higher gas productivity than HSW.
Zhang et al. [26,27]	2020, 2021	Numerical simulation	Studied the performance of gas hydrate development by combining radial lateral wells with depressurization.	Radial lateral wells can improve gas recovery rates in the early stages of production and slow down secondary hydrates generation. The recovery rate of hydrates is linearly related to the lateral length.
Zhang et al. [28]	2022	Experimental	Experimental studies were conducted on the depressurization and extraction of hydrated sediments in both gas-rich and water-rich using vertical and radial lateral wells, respectively.	When extracting rich gas hydrate sediments, the gas production behavior of vertical and radial lateral wells is almost the same. When extracting rich water hydrate sediments, the cumulative gas production of radial lateral well increased by 20.16% compared to vertical well.
Wan et al. [29]	2024	Numerical simulation	A numerical evaluation was conducted on the gas production capacity of Class-1 type hydrate reservoirs using different radial lateral well deployment schemes.	Compared to a single vertical well, the cumulative gas production of a radial lateral well increased by approximately 208.53%.

2. Methodology

2.1. Method and Process

Taking China's first offshore NGH testing production as an example, the NGH development simulation software TOUGH + HYDRATE V1.0 was adopted to establish an ideal interlayer heterogeneity model based on SHSC4 well logging curve data. The gas production data of the site was fitted to verify the reliability of the numerical model. This work predicted and compared the gas and water production behavior of RLW and HSW with different completion lengths when they deployed at different layers, with a fixed production pressure difference of 6 MPa and continuous production for 360 days. The methodology flow chart is shown in Figure 1.
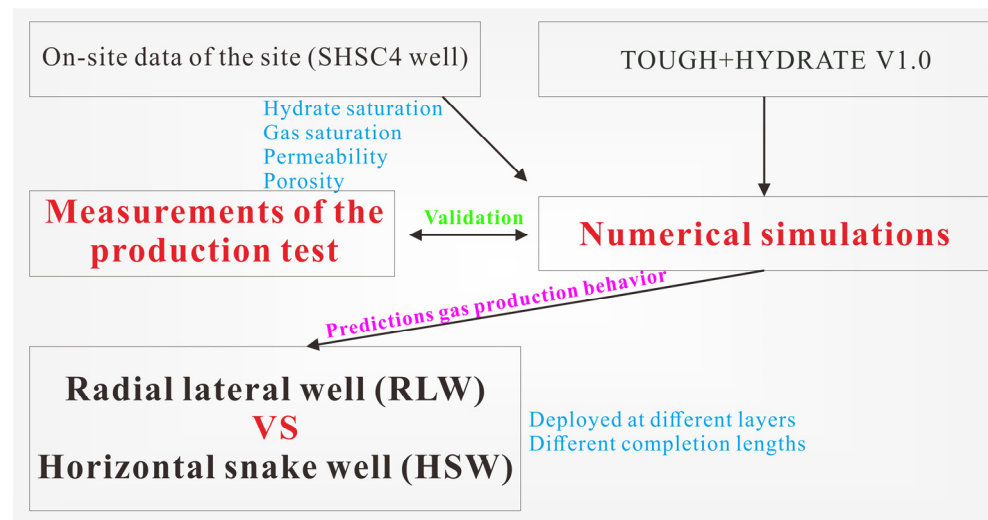

Figure 1. Methodology flow chart.

2.2. Geological Background

The SHSC4 well is located in the Baiyun sag (Figure 2). The water depths at this site are about 1266 m, and the seabed temperature is around 3.33–3.73 °C, with the geothermal gradient ranging from 45 to 67 °C/km [7,30]. The hydrate reservoir consists of three parts: the first layer is the natural gas hydrate layer rich in hydrates and water (GHBL, 201–236 mbsf); the second layer is the three-phase layer containing hydrates, high saturation free gas, and water (TPL, 236–251 mbsf); and the third layer is the free gas layer composed of water and low saturation free gas (FGL, 251–278 mbsf) [7].

2.3. Simulator Code

TOUGH + HYDRATE V1.0 is a well-known natural gas hydrate simulation code which considers the interactions between hydrate phases, multiphase flow, and heat transfer. It can accurately describe the dynamic changes in temperature, pressure, and saturation during the formation or dissociation process of hydrates [31]. The parallel version of this code was used for this work and adopted the equilibrium model for simulating hydrate extraction [32,33]. The main governing equation of this code is briefly introduced as follows [31]:

1. Mass conservation equation

The definition of the flow control equation for multicomponent fluid that follow mass conservation is as follows:

$$\frac{d}{dt}\int_{V_n} M^\kappa dV = \int_{\Gamma_n} F^\kappa \cdot \mathbf{n} d\Gamma + \int_{V_n} q^\kappa dV \tag{1}$$

In this equation, M^κ is the mass accumulation of components, F^κ is the flux, and q^κ is the source/sink ratio.

2. Energy conservation equation

The definition of the heat flow control equation follows energy conservation as follows:

$$\frac{d}{dt} \int_{V_n} M^\theta dV = \int_{\Gamma_n} F^\theta \cdot \mathrm{n} d\Gamma + \int_{V_n} q^\theta dV \tag{2}$$

In this equation, θ is the heat component, M^θ is the heat accumulation, F^θ is the flux, and q^θ is the source/sink ratio.
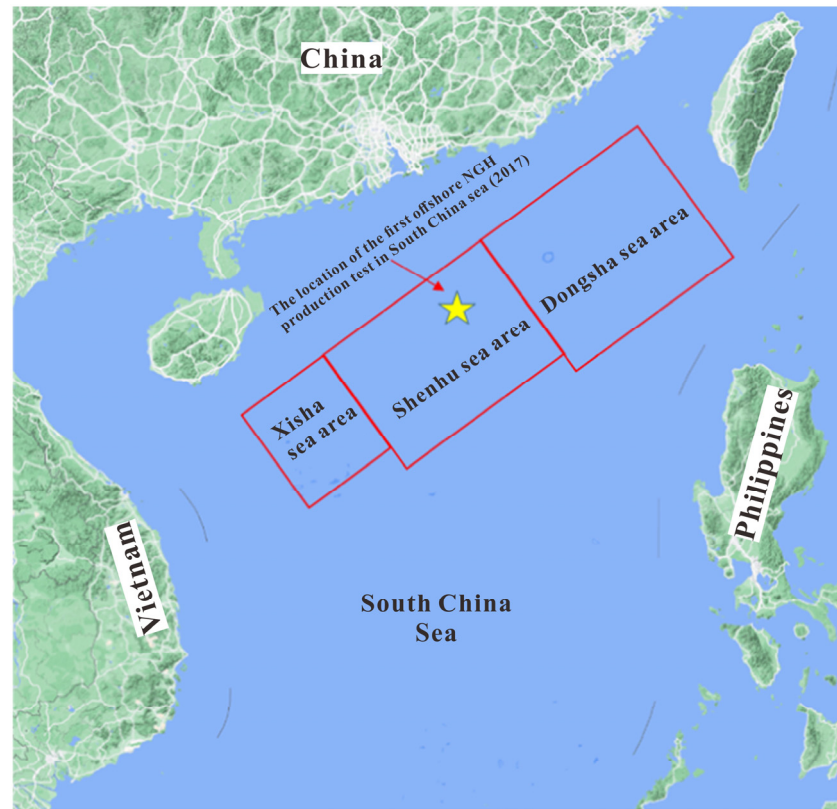

Figure 2. SHSC well site location [14]. (Adapted with permission from Hao, et al. Dynamic analysis of exploitation of different types of multilateral wells of a hydrate reservoir in the South China sea. *Energy & Fuels* 2022, *36*, 6083–6095., Copyright 2022 American Chemical Society.).

2.4. Model Discretization and Simulation Scenarios

A schematic diagram of the model is shown in Figure 3a. The *x*-*y* plane domain was discretized into 13,221 grids, and the model's *z*-axis was divided into 81 layers, with a total of 1,070,901 grids (Figure 3b). Hydrate dissociation is active near the wellbore and local refinement grids facilitate the capture of dynamic variations of temperature, pressure, and hydrate saturation. The minimum grid around the wellbore was set to *x* = 2.0 m, *y* = 2.0 m, and *z* = 1.0 m. This work established a total of nineteen simulation cases: (1) Single vertical well: the single vertical well with a length of 70 m was placed at the center of the model (Figure 3c). (2) Radial lateral well (RLW): Three simulation schemes: RLW-4 laterals, RLW-6 laterals, and RLW-8 laterals were established, each radial laterals well with a length of 357.05 m, 467.47 m, and 639.67 m respectively; RLW-4 laterals, RLW-6 laterals, and RLW-8 laterals were deployed at the middle of the three layers, respectively, (Figure 3d). (3) Horizontal snake well (HSW): Three simulation schemes: HSW-1 circle, HSW-1.5 circles, and HSW-2 circles were established, each horizontal snake well with a length of 357.05 m, 467.47 m, and 639.67 m respectively; HSW-1 circle, HSW-1.5 circles, HSW-2 circles were deployed at the middle of the three layers respectively (Figure 3e). Table 2 lists the detailed settings of the simulation scheme.
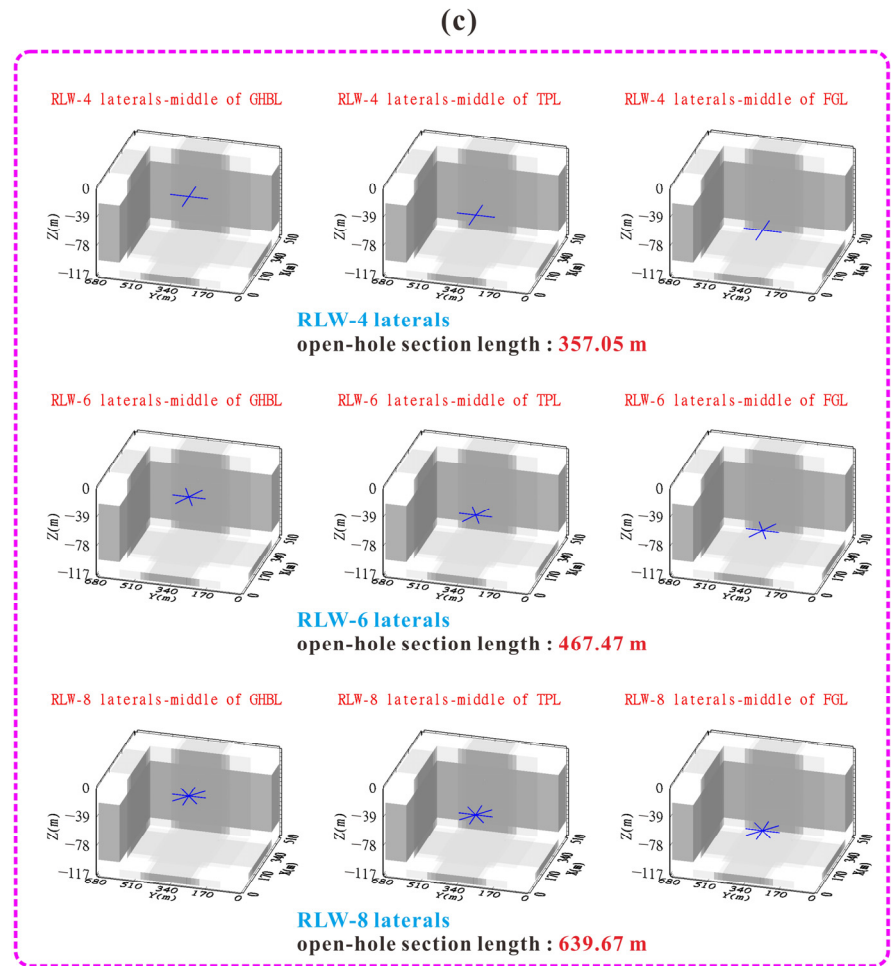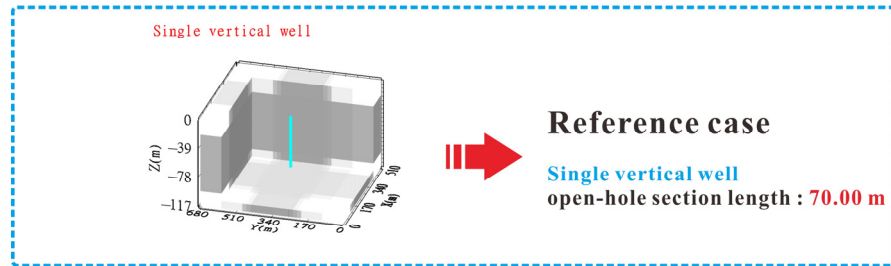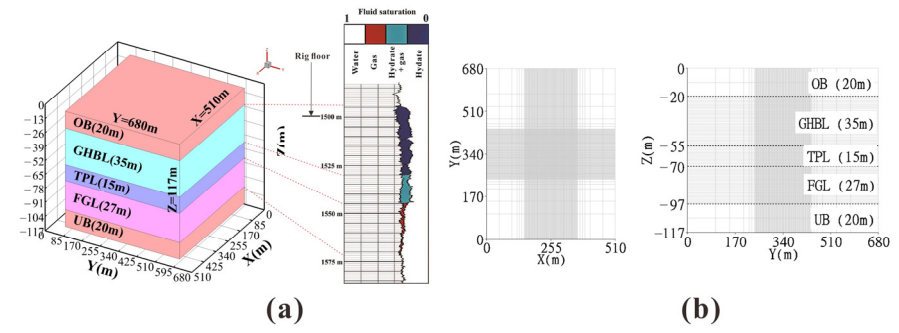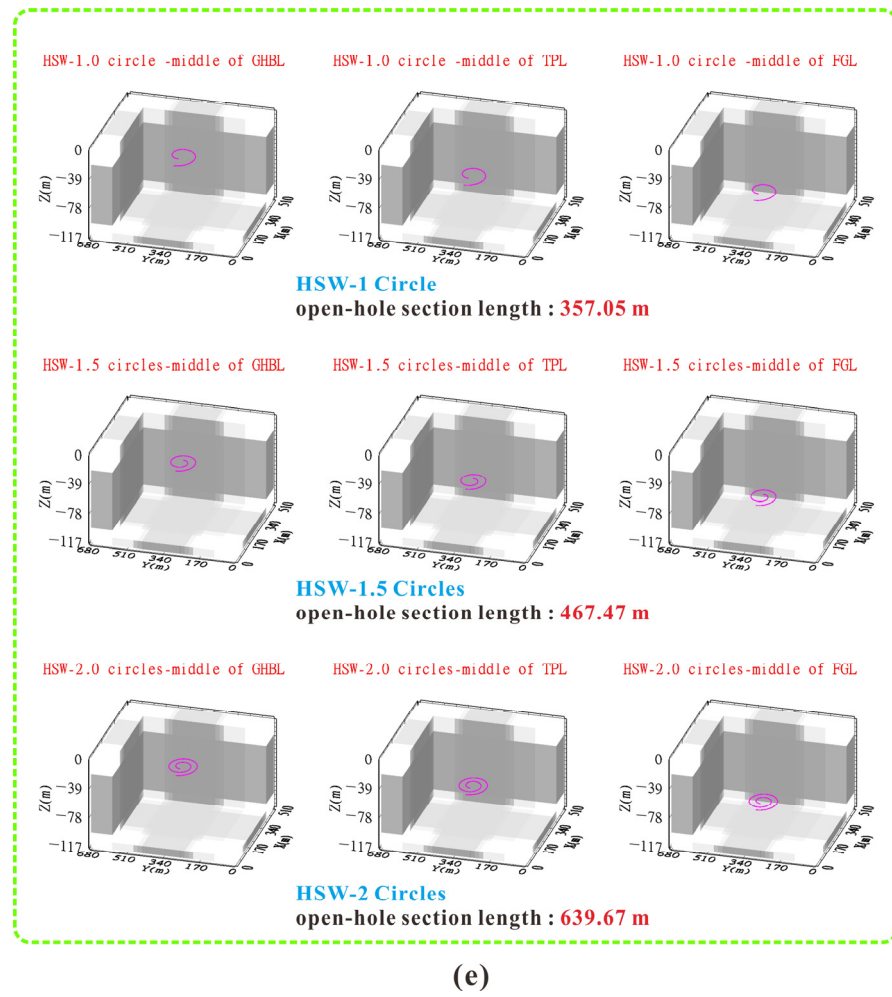
Figure 3. *Cont.*

Figure 3. Schematic diagram of the model and well types: (**a**) geological model and Logging curve of SHSC-4 well. (**b**) Model mesh. (**c**) Schematic diagram of vertical well. (**d**) Schematic diagram of radial lateral well. (**e**) Schematic diagram of horizontal snake well.

Table 2. Detailed settings of the simulation scheme.

Case	Parameter Settings			
	L/(m)	*l*/(m)	*n*	Wellbore Location
Single vertical well	70	-	-	-
RLW-4 laterals	357.05	89.26	4	
RLW-6 laterals	467.47	77.91	6	
RLW-8 laterals	639.67	79.95	8	Middle of
HSW-1 circle	357.05	-	-	GHBL/TPL/FGL
HSW-1.5 circles	467.47	-	-	
HSW-2 circles	639.67	-	-	

Note: *L* is the open-hole completion length of wellbore; *l* is the length of each lateral wellbore; *n* is the quantity of lateral wellbore.

2.5. Model Initialization

GHBL, TPL, and FGL were initialized as individual subdomains, and the key was to maintain consistent heat flux between the contact surfaces of the subdomains. Finally, we combined the initialized subdomains as shown in Figure 4 [34–37] and set fixed temperatures and pressures at the top and bottom of the model to establish Dirichlet boundary conditions [38]. When the RLW and HSW were deployed at the middle of three layers, re-

spectively, the production pressure difference between the wellbore grids and the reservoir was set to 6 MPa. In this work, the wellbore radius of the single vertical well was set to be 0.1 m, and the RLW and HSW were set to be 0.05 m [25].
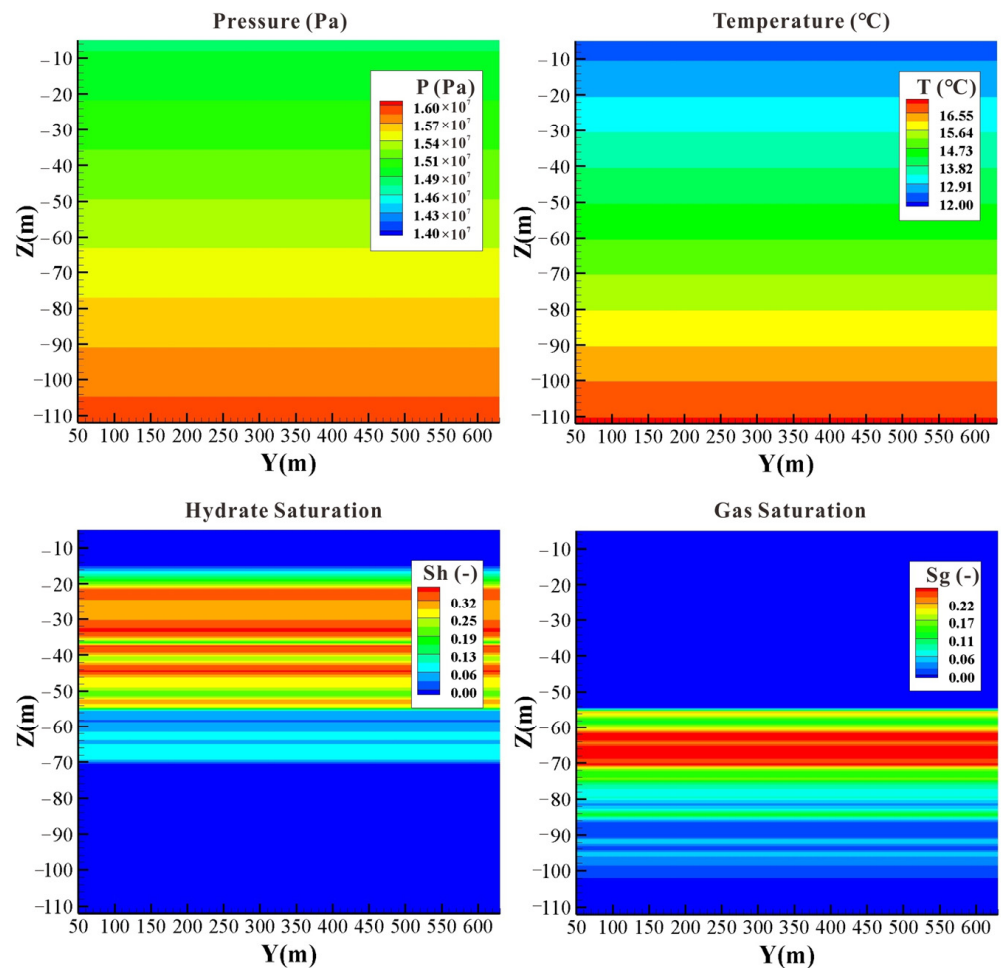

Figure 4. Model's initial conditions.

The physical properties of reservoirs, such as porosity, permeability, and saturation, were initialized based on the on-site data [7]. Since there was no information for the OB and UB, we assumed that their permeability was 2.0 mD and their porosity was 0.3. Table 3 provides the initial values of the main parameters.

Table 3. Initial values of the main parameters.

Parameter	Value and Unit	Data Sources
Overburden (OB) and Underburden (UB)'s thickness	20 m	[39]
GHBL's thickness	35 m	[40]
TPL's thickness	15 m	[40]
FGL's thickness	27 m	[40]
OB and UB's permeability	2.0 mD	-
GHBL's permeability	2.9 mD	[40]
TPL's permeability	1.5 mD	[40]
FGL's permeability	7.4 mD	[40]
OB and UB's porosity	0.30	[40]

Table 3. *Cont.*

Parameter	Value and Unit	Data Sources
GHBL's porosity	0.35	[40]
TPL's porosity	0.33	[40]
FGL's porosity	0.32	[40]
GHBL and TPL's hydrate saturation FGL's gas saturation	Extract from logging curve (Figure 3a)	[7]
Single vertical wellbore radius	0.1 m	[25]
Radial lateral wellbore radius	0.05 m	[25]
Horizontal snake wellbore radius	0.05 m	[25]
Production pressure difference	6.0 MPa	-
Salinity	3.0%	[40–42]
Grain density	2650 kg/m^3	[40–42]
Geothermal gradient	46 °C/km	[30]
Grain specific heat	1000 J$\cdot$kg$^{-1}\cdot$K^{-1}	[40–42]
Dry thermal conductivity	1.0 W$\cdot$m$^{-1}\cdot$K^{-1}	[40–42]
Wet thermal conductivity	3.1 W$\cdot$m$^{-1}\cdot$K^{-1}	[40–42]
Capillary pressure model	$P_{cap} = -P_0\left[(S^*)^{-1/\lambda} - 1\right]^{1-\lambda}$, $S^* = \frac{(S_A - S_{irA})}{S_{mxA} - S_{irA}}$	-
Maximum aqueous saturation S_{mxA}	1	[40–42]
Porosity distribution index λ	0.45	[40–42]
Initial capillary pressure P_0	10^4 Pa	[40–42]
Relative permeability model	$K_{rA} = [(S_A - S_{irA})/(1 - S_{irA})]^{nA}$, $K_{rG} = [(S_G - S_{irG})/(1 - S_{irA})]^{nG}$	-
Aqueous phase permeability reduction index n_A	3.5	[41]
Gas phase permeability reduction index n_G	2.5	[41]
Irreducible gas saturation S_{irG}	0.03	[41]
Irreducible aqueous saturation S_{irA}	0.30	[41]

2.6. Model Validation

Model validation is a crucial step in numerical simulation research. According to the data released by Li et al., the gas production of China's first offshore natural gas hydrate trial production is shown in Table 4 [43].

Table 4. Gas production of the first offshore NGH test production in China.

Duration/d	Cumulative Gas Volume/10^4 m^3	Gas Rate/10^3 m$^3\cdot$d^{-1}
0–8	12.80	16.00
9–16	3.20	4.00
17–22	2.37	3.95
23–31	2.71	2.98
32–42	2.42	2.20
43–60	7.40	4.11

The single vertical well was deployed at the center of the model with a length of 70 m, the completion interval was −201 to −271 mbsf (consistent with the model's −21 m to −91 m), and the wellbore grid had a production pressure difference of 3 MPa [44]. The position of the vertical well is shown in Figure 5.

Figure 6 shows the fitting results of gas production. It can be seen that the fitting results of simulated gas production and trial production data were within an acceptable range. According to the fitting results, this model can serve as the basic model for subsequent research.
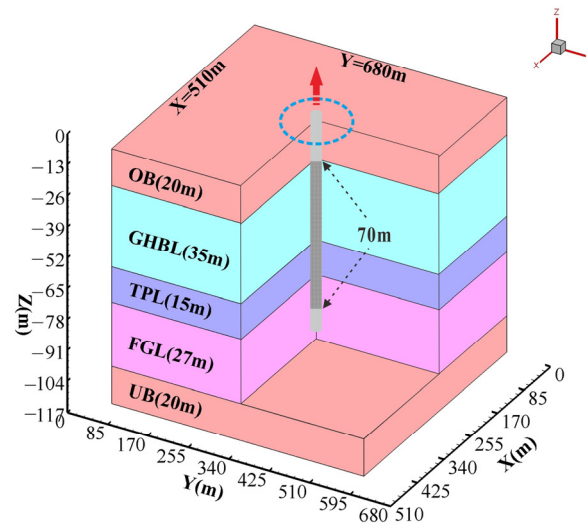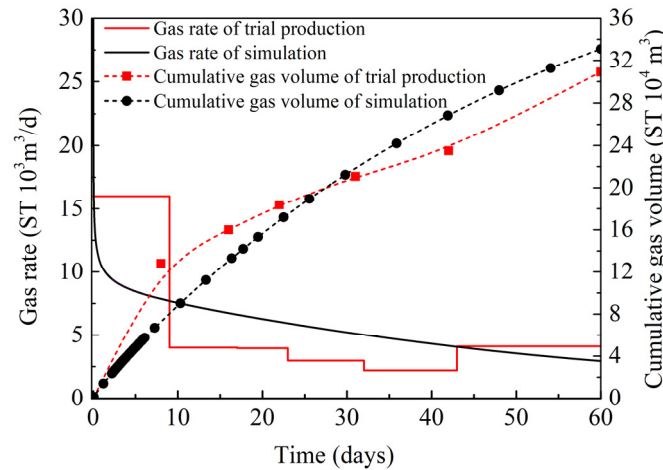
Figure 5. Vertical well position.

Figure 6. On-site gas production fitting.

3. Results and Discussion

3.1. RLW and HSW Deployed at GHBL

3.1.1. Evolution of Gas and Water Characteristics

Figure 7a,b shows the variation curves of gas production rate (Q_g) and cumulative gas production (V_g) with different RLW and HSW design deployment at the middle of GHBL. The gas production rate curves of these two well types can be divided into two stages. The existence of solid hydrates results in a lower effective permeability of the GHBL layer, therefore Q_g remains at a relatively low level in the early stages of production. After 90 days of depressurization, as the hydrates dissociation around the wellbore improves the seepage conditions, the free gas from TPL suddenly increases Q_g and V_g, leading to the second stage of production. Subsequently, they decrease as the driving force weakens. After 360 days of depressurization, the V_g of RLW-4 laterals, RLW-6 laterals, RLW-8 laterals, HSW-1 circle, HSW-1.5 circles, and HSW-2 circles were 453.83×10^4, 596.20×10^4, 731.84×10^4, 514.16×10^4, 644.57×10^4, and 849.53×10^4 ST m^3, compared to the single vertical well, and increased by 124.22%, 163.19%, 200.31%, 140.73%, 176.42%, and 232.53%, respectively. The results show that RLW and HSW can increase the drainage area and significantly improve production capacity. Figure 7c,d shows the variation curves of the water production rate (Q_w) and the gas-to-water ratio (R_{gw}). Compared with the single vertical well, the solid hydrates around the RLW and HSW's wellbore dissociation under the driving force, and the water produced via hydrates dissociation enters the wellbore, causing the Q_w to show a

stable period before 90 days. With the free gas from TPL beginning to enter the wellbore, the Q_w suddenly decreases at 90 days. As a critical index for evaluating the efficiency of hydrate extraction, a higher R_{gw} (ST m^3 of CH$_4$/ST m^3 of water) implies better economically feasibility. When these two types of wells were deployed at GHBL, their R_{gw} was ultimately stable at around 100. Table 5 shows the gas production of these well types.
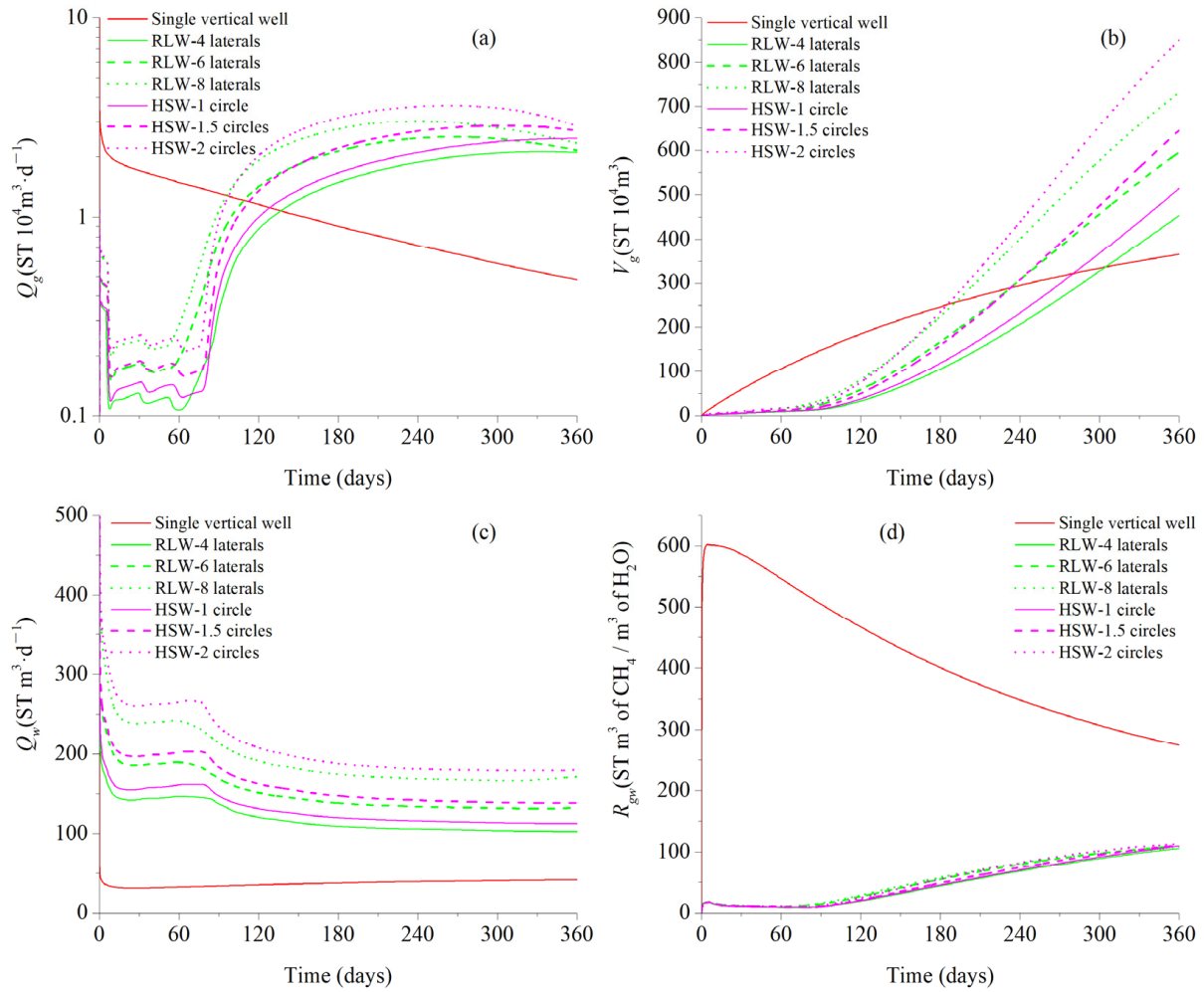

Figure 7. Gas and water production curves of RLW and HSW deployed at GHBL: (**a**) gas production rate Q_g. (**b**) Cumulative gas production V_g. (**c**) Water production rate Q_w. (**d**) Gas-to-water ratio R_{gw}.

Table 5. Gas production of RLW and HSW deployed at GHBL.

Case	Average Q_g (10^4 m^3/d)	V_g (10^4 m^3)	Compared to VW (Ref)
HSW-2 circles	2.36	849.53	232.53%
RLW-8 laterals	2.03	731.84	200.31%
HSW-1.5 circles	1.79	644.57	176.42%
RLW-6 laterals	1.66	596.20	163.19%
HSW-1 circle	1.43	514.16	140.73%
RLW-4 laterals	1.26	453.83	124.22%
Single vertical well	1.01	365.35	100.00%

3.1.2. Physical Characteristics of the Reservoir

The internal wellbore of HSW and the intersection of laterals in RLW had larger pressure drop areas (Figure 8a), which was due to the pressure superposition. This phenomenon was consistent with the findings of Jin et al. [15]. Compared with the well types deployed at TPL and FGL, the well types deployed at GHBL had a larger pressure gradient. This is because the presence of solid hydrates reduces the effective permeability of the reservoir, and allows for effective pressure propagation. The TPL and FGL contain free gas and the expansion effect of the gas limits the propagation of pressure, resulting in a smaller pressure gradient. Low-temperature areas were formed near the wellbore (Figure 8b) due to the heat absorption caused by the dissociation of hydrates (Figure 8c). Corresponding to the pressure field diagram, the internal wellbore of HSW and the intersection of laterals in RLW had a larger low-temperature area and hydrate dissociation range. A certain amount of gas was accumulated around the wellbore after 360 days of depressurization (Figure 8d).
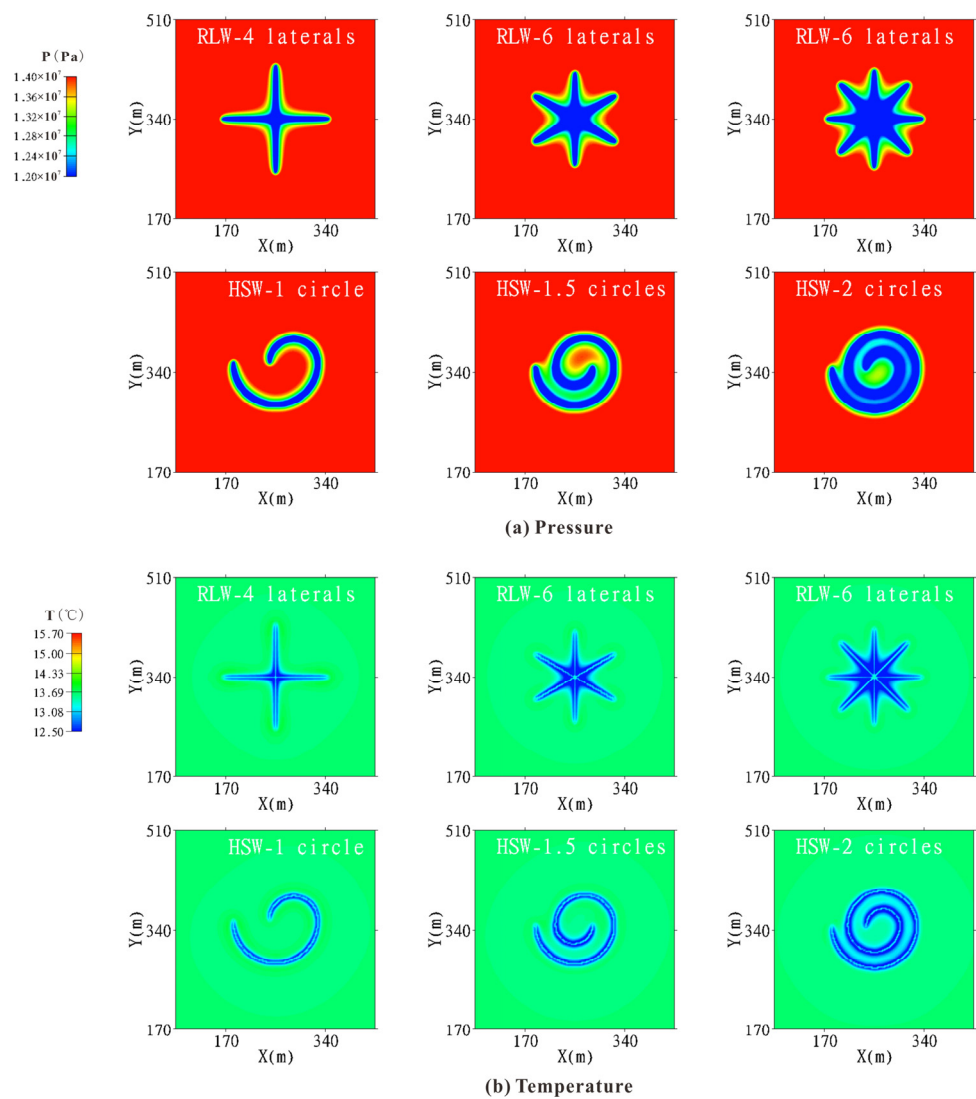

Figure 8. *Cont.*
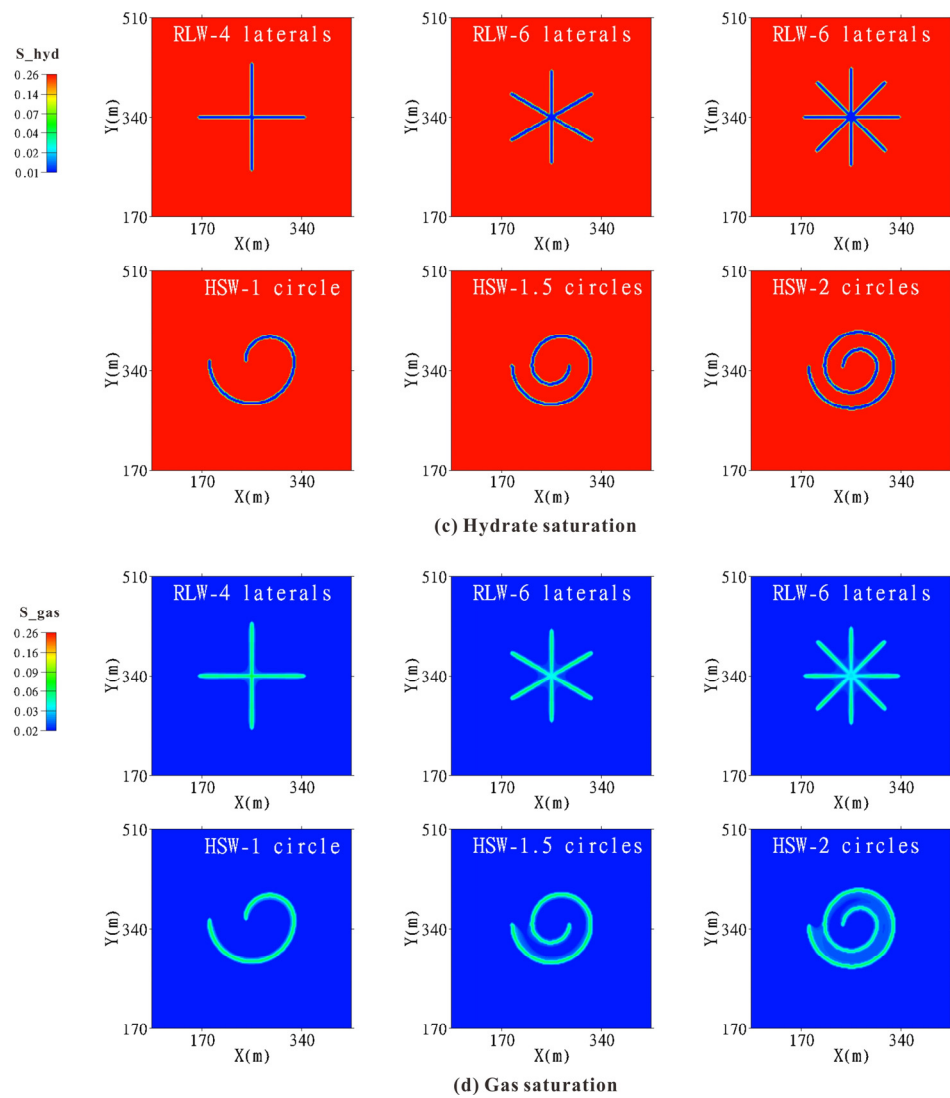
Figure 8. Physical characteristics distribution diagram of RLW and HSW deployed at GHBL.

3.2. RLW and HSW Deployed at TPL

3.2.1. Evolution of Gas and Water Characteristics

Figure 9a,b shows the variation curves of Q_g and V_g with different RLW and HSW design deployments at the middle of TPL. The Q_g of these two well types gradually decreased after reaching its peak value in the initial stage. Even so, its Q_g and V_g were the highest compared to the well types deployed at GHBL and FGL, which was because it can simultaneously recover hydrate dissociation gas from GHBL and free gas from TPL and FGL. Wan et al. also found the same results in previous studies [29]. After 360 days of depressurization, the V_g of RLW-4 laterals, RLW-6 laterals, RLW-8 laterals, HSW-1 circle, HSW-1.5 circles, and HSW-2 circles were 1215.12 × 10^4, 1294.38 × 10^4, 1356.88 × 10^4, 1305.72 × 10^4, 1463.54 × 10^4, and 1554.73 × 10^4 ST m^3, compared to the single vertical well, increased by 332.59%, 354.29%, 400.58%, 357.39%, 371.39%, and 425.54%, respectively. The results showed that the well types deployed at TPL had excellent production performance. It is worth noting that, similar to the wells deployed at GHBL, the overall production capacity of the HSW well was better than that of RLW, especially the production capacity of the HSW-1 circle was better than that of RLW-4 and RLW-6 laterals. This may be due to the smaller distance between the wellbore of HSW with spiral distribution, resulting in a larger range of pressure superposition and stronger synergistic production effects between wellbore. In this case, the reservoir at the root of the RLW laterals wellbore formed a certain

amount of secondary hydrates, as shown in Figure 10c. Figure 9c,d shows the variation curves of Q_w and R_{gw}. When these well types were deployed at TPL, their Q_w was slightly lower overall compared to those deployed at GHBL and FGL. This was because a lot of free gas entered the wellbore, which affects water production; their R_{gw} was ultimately stable at around 200. Table 6 shows the gas production of these well types.
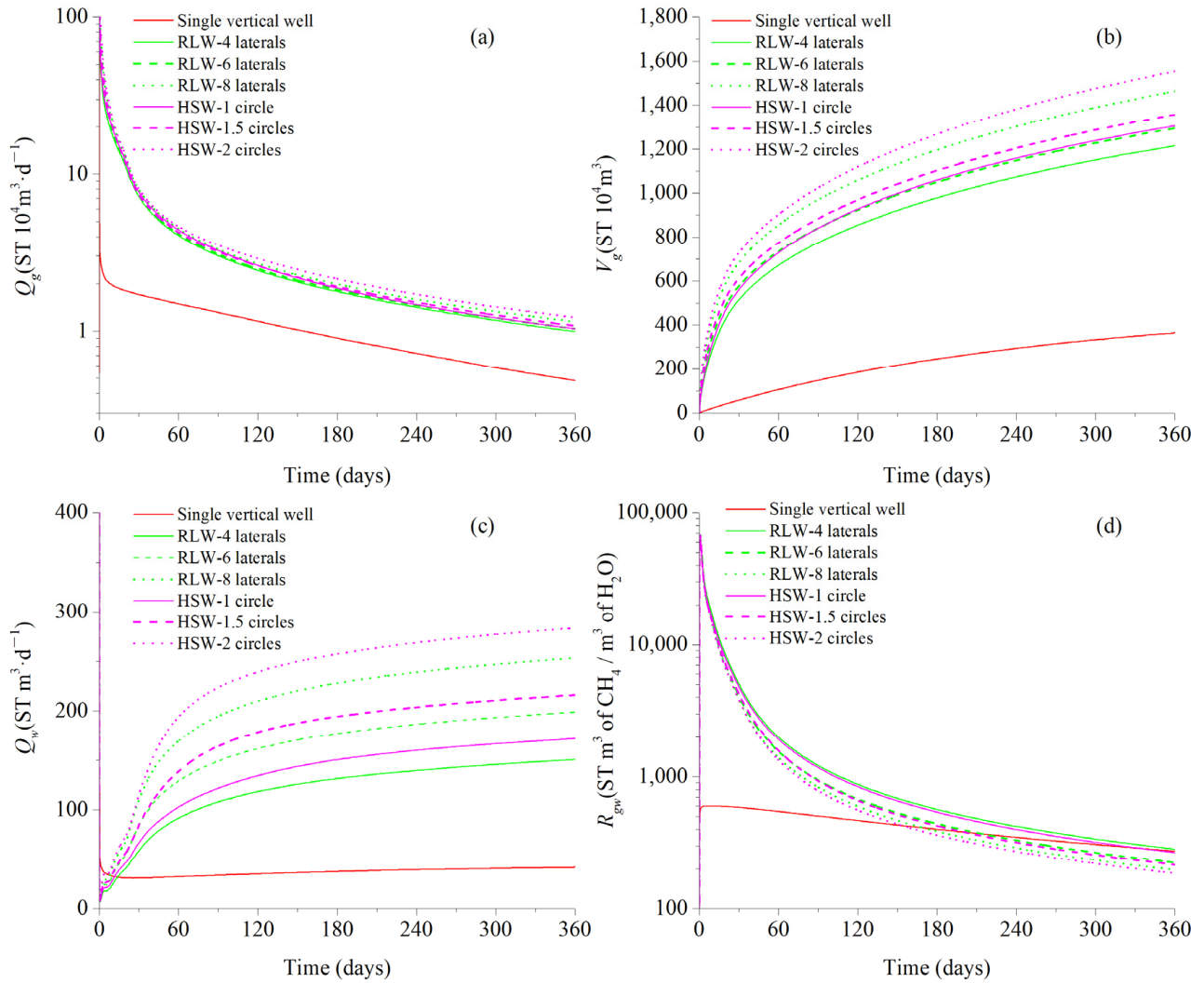

Figure 9. Gas and water production curves of RLW and HSW deployed at TPL: (**a**) gas production rate Q_g. (**b**) Cumulative gas production V_g. (**c**) Water production rate Q_w. (**d**) Gas-to-water ratio R_{gw}.

Table 6. Gas production of RLW and HSW deployed at TPL.

Case	Average Q_g (10⁴ m³/d)	V_g (10⁴ m³)	Compared to VW (Ref)
HSW-2 circles	4.32	1554.73	425.54%
RLW-8 laterals	4.07	1463.54	400.58%
HSW-1.5 circles	3.77	1356.88	371.39%
HSW-1 circle	3.63	1305.72	357.39%
RLW-6 laterals	3.60	1294.38	354.29%
RLW-4 laterals	3.38	1215.12	332.59%
Single vertical well	1.01	365.35	100.00%

3.2.2. Physical Characteristics of the Reservoir

The pressure superposition effect results in larger low-pressure area areas at the internal wellbore of HSW and the intersection of laterals in RLW (Figure 10a). The Joule–Thomson effect promotes the formation of low-temperature areas near wellbore reservoirs (Figure 10b). The reservoir at the root of the RLW laterals wellbore formed a certain amount of secondary hydrates after 360 days of depressurization (Figure 10c). Moreover, due to long-term mining, the surrounding areas of these well types formed corresponding low-saturation gas areas (Figure 10d).
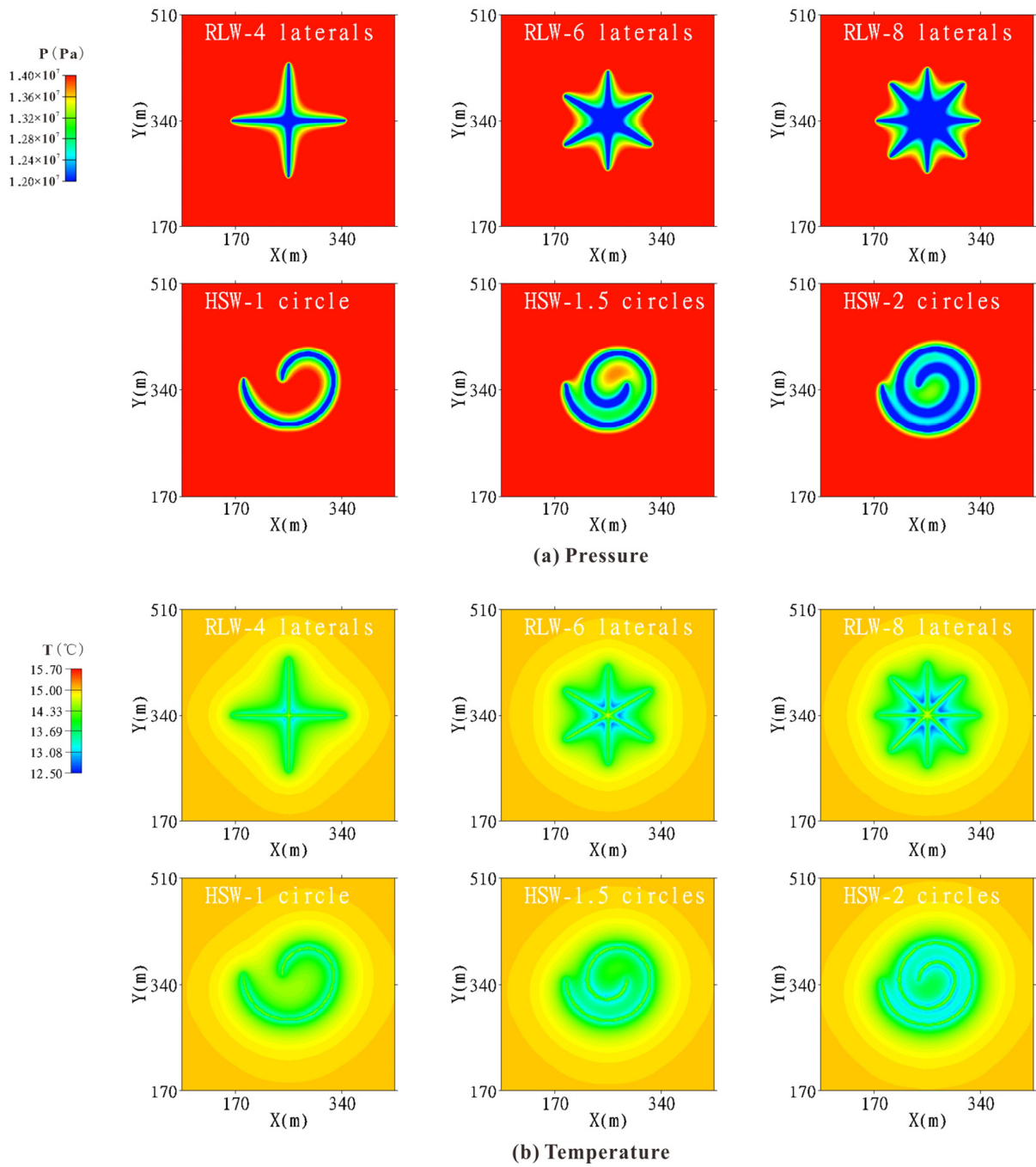

Figure 10. *Cont.*

(c) Hydrate saturation
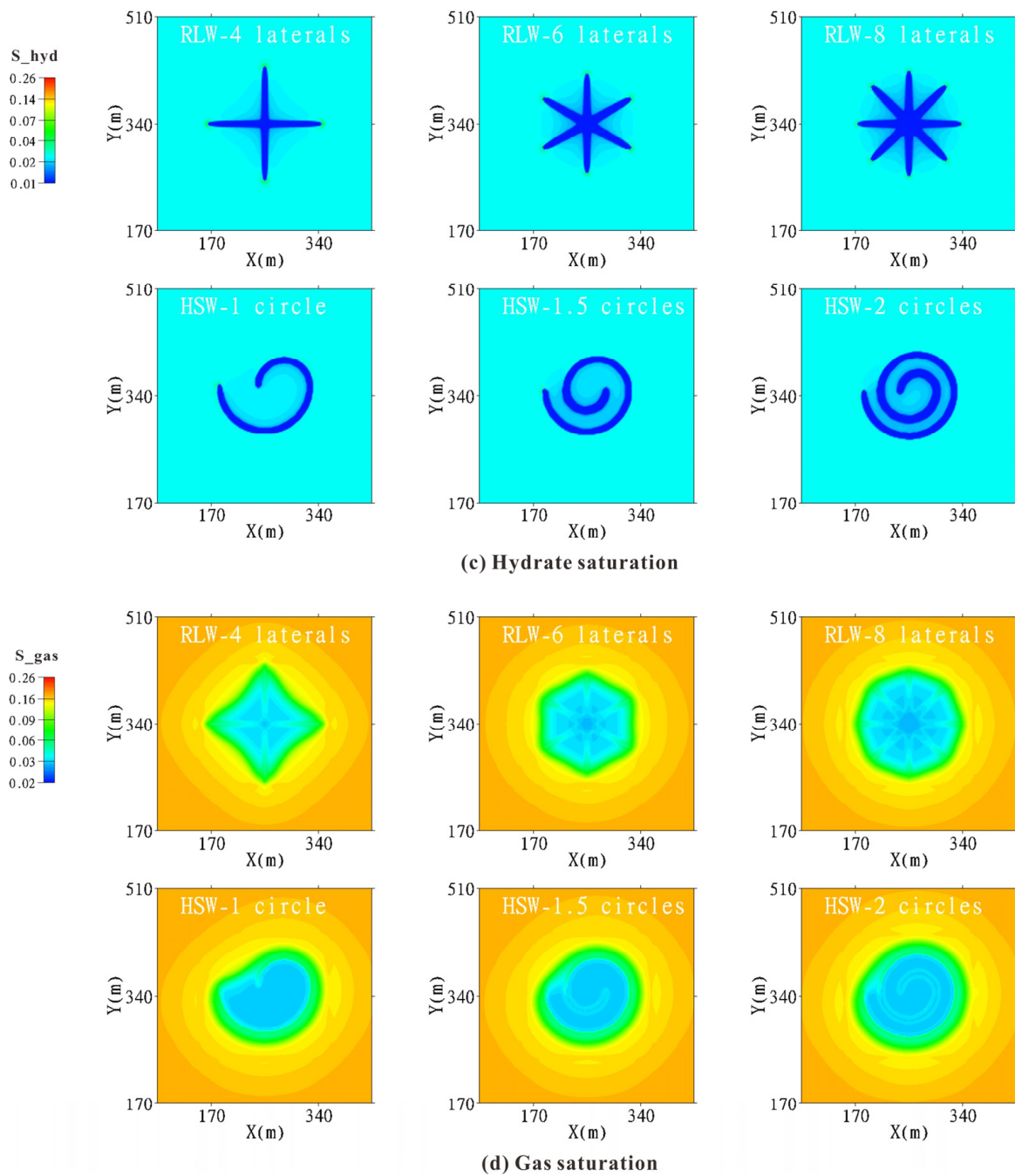

(d) Gas saturation

Figure 10. Physical characteristics distribution diagram of RLW and HSW deployed at TPL.

3.3. RLW and HSW Deployed at FGL

3.3.1. Evolution of Gas and Water Characteristics

Figure 11a,b shows the variation curves of Q_g and V_g with different RLW and HSW design deployments at the middle of FGL. After about eight days of depressurization, the Q_g of these two well types suddenly increased with the free gas from TPL entering the wellbore and gradually decreased with the weakening of the driving force. After 360 days of depressurization, the V_g of RLW-4 laterals, RLW-6 laterals, RLW-8 laterals, HSW-1 circle, HSW-1.5 circles, and HSW-2 circles were 1027.71×10^4, 1141.27×10^4, 1303.45×10^4, 1148.70×10^4, 1303.45×10^4, and 1396.74×10^4 ST m^3, compared to the single vertical well, increased by 281.29%, 312.38%, 356.77%, 314.41%, 330.46%, and 382.30%, respectively. Similar to the wells deployed at GHBL and TPL, the overall production capacity of HSW well was better than that of RLW and the production capacity of HSW-1 circle was better

than that of RLW-4 and RLW-6 laterals again. Figure 11c,d shows the variation curves of Q_w and the R_{gw}. Compared with the well types deployed at GHBL and TPL, the well types deployed at FGL had a slightly higher water production rate because it had a higher water saturation of about 93%, and their R_{gw} was ultimately stable at around 100 to 200. Table 7 shows the gas production of these well types.
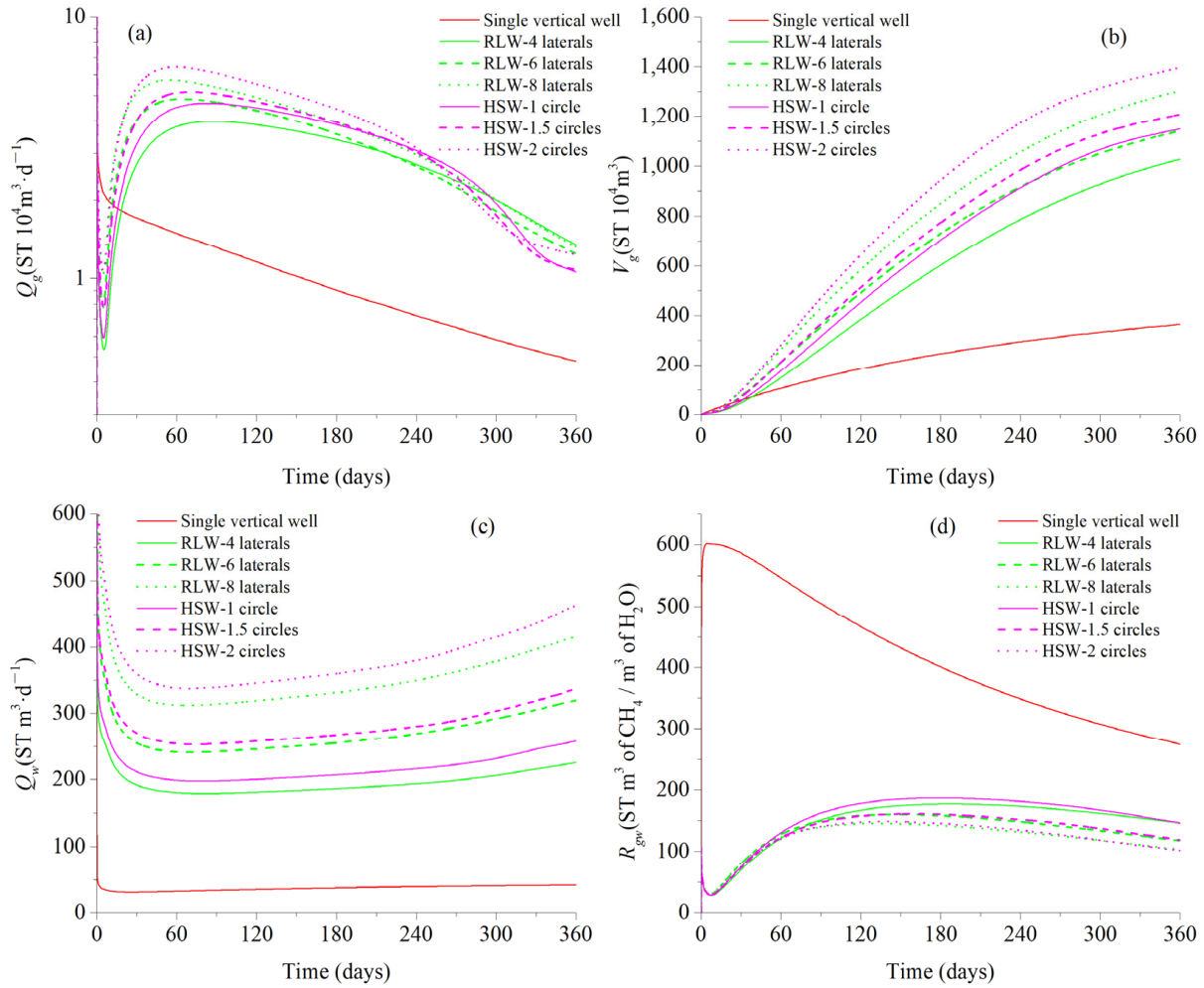

Figure 11. Gas and water production curves of RLW and HSW deployed at FGL: (**a**) gas production rate Q_g. (**b**) Cumulative gas production V_g. (**c**) Water production rate Q_w. (**d**) Gas-to-water ratio R_{gw}.

Table 7. Gas production of RLW and HSW deployed at FGL.

Case	Average Q_g (10^4 m^3/d)	V_g (10^4 m^3)	Compared to VW (Ref)
HSW-2 circles	3.88	1396.74	382.30%
RLW-8 laterals	3.62	1303.45	356.77%
HSW-1.5 circles	3.35	1207.33	330.46%
HSW-1 circle	3.19	1148.70	314.41%
RLW-6 laterals	3.17	1141.27	312.38%
RLW-4 laterals	2.85	1027.71	281.29%
Single vertical well	1.01	365.35	100.00%

3.3.2. Physical Characteristics of the Reservoir

Due to the superimposed pressure drop, the internal wellbore of HSW and the intersection of laterals in RLW had larger pressure drop areas (Figure 12a). Compared with the well types deployed at GHBL and TPL, the gas expansion effect weakened pressure propagation when the well types deployed at FGL. There were no low-temperature areas or secondary hydrates formed around the wellbore (Figure 12b,c), which was because FGL has a higher formation temperature. Additionally, a low saturation of free gas accumulated around these well type's wellbores (Figure 12d).
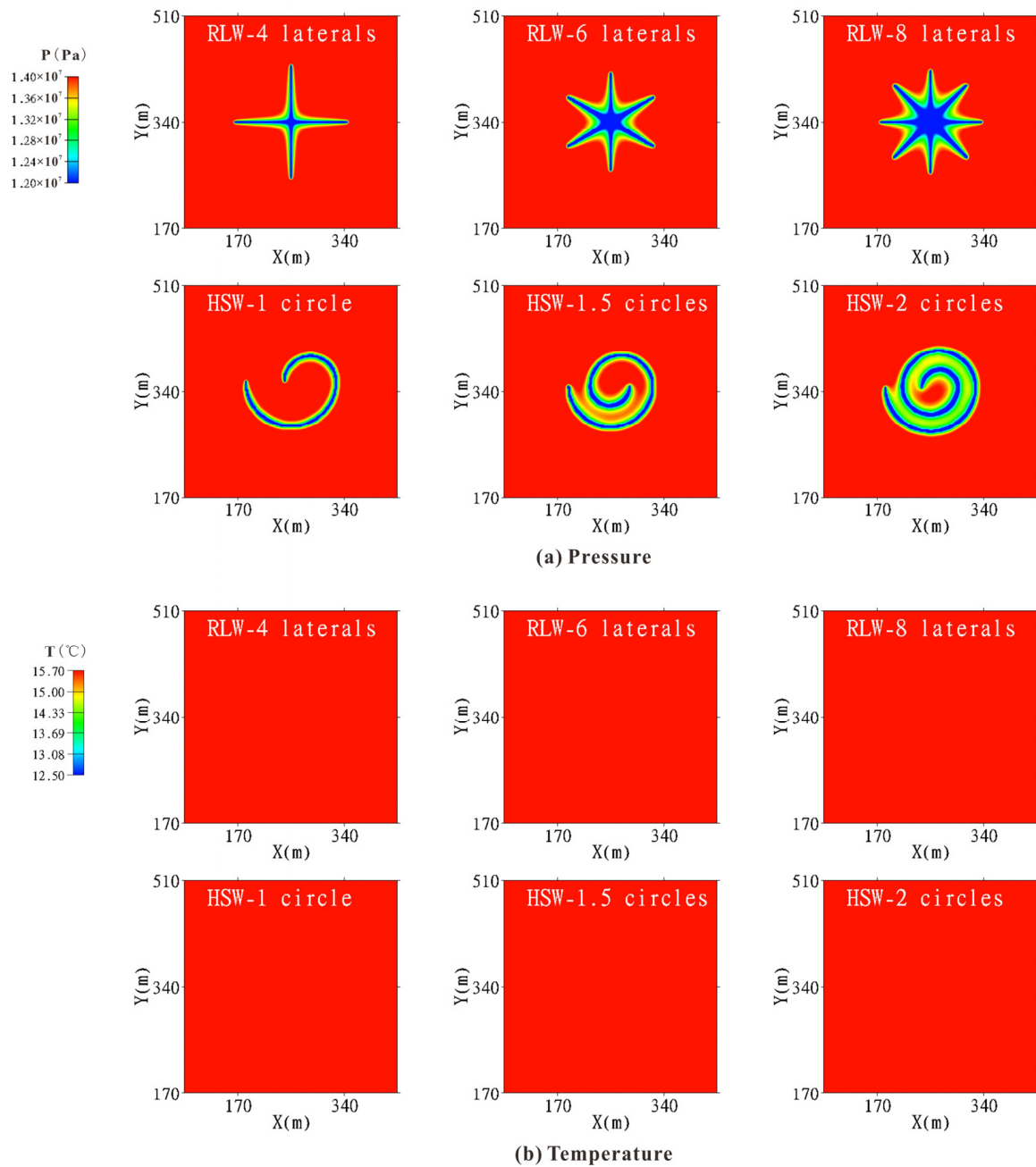

(a) Pressure

(b) Temperature

Figure 12. *Cont.*

(c) Hydrate saturation
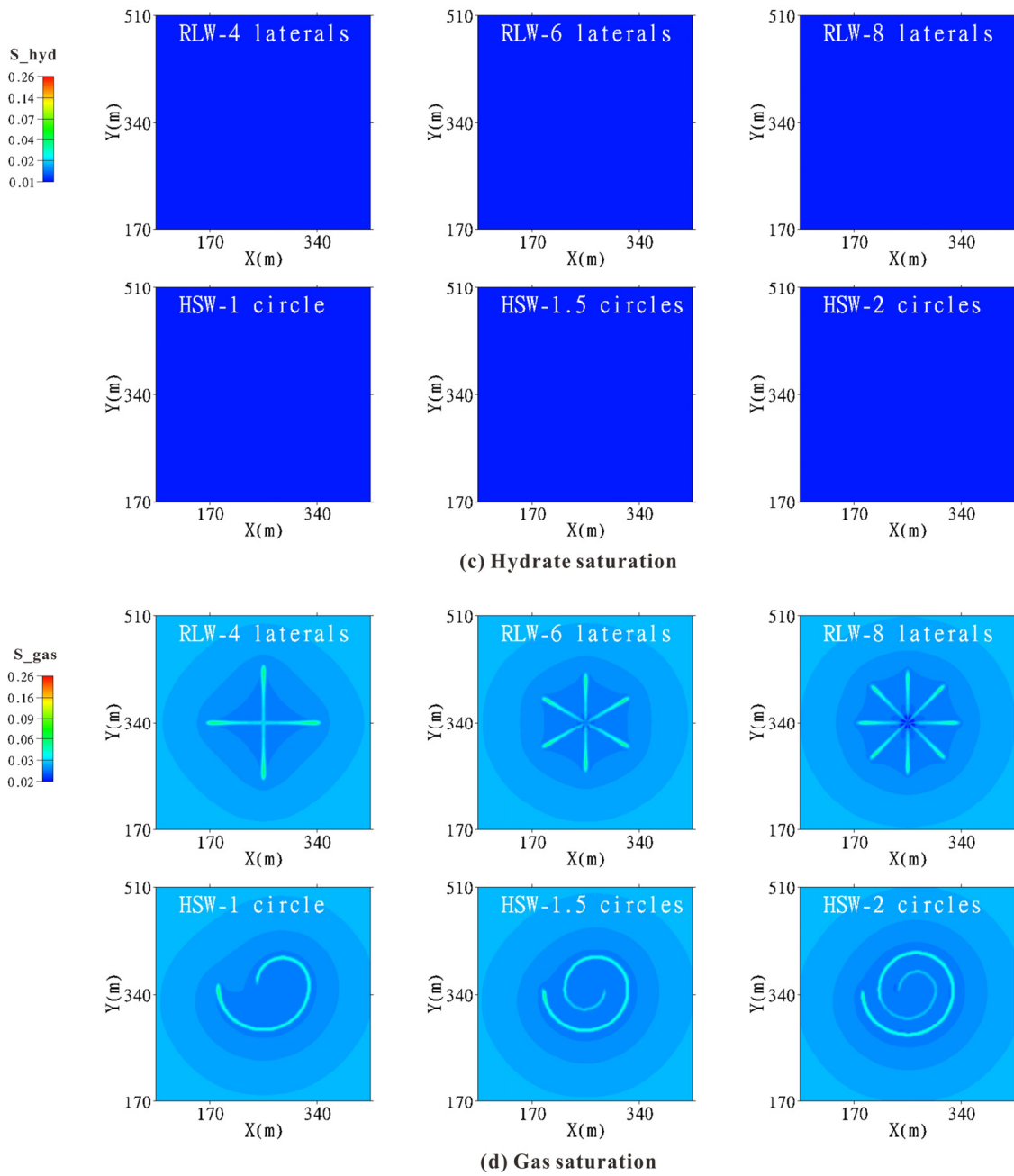

(d) Gas saturation

Figure 12. Physical characteristics distribution diagram of RLW and HSW deployed at FGL.

3.4. Discussion

3.4.1. Comparison of Production Capacity

The average Q_g and average R_{gw} are commonly used to evaluate production capacity. Figure 13 depicts the average Q_g and average R_{gw} of these well types during the 360-day production period. When these well types are deployed at GHBL, the average Q_g slowly increases with the dissociation of solid hydrates during production. Due to the synergistic pressure reduction effect between wellbores, the HSW well type performs better under the same completion length. When these well types are deployed at TPL or FGL, their average Q_g decreases with production as the driving force weakens. Similarly, due to the synergistic pressure reduction effect between wellbores, the HSW well type performs better. In addition, these well types have the best average R_{gw} performance when deployed at the TPL. Due to the production capacity, they may not be completely proportional to the well

length. Therefore, the specific production index *J* is adopted as a supplementary indicator, which is mainly affected by the well types and the definition is as follows [9]:
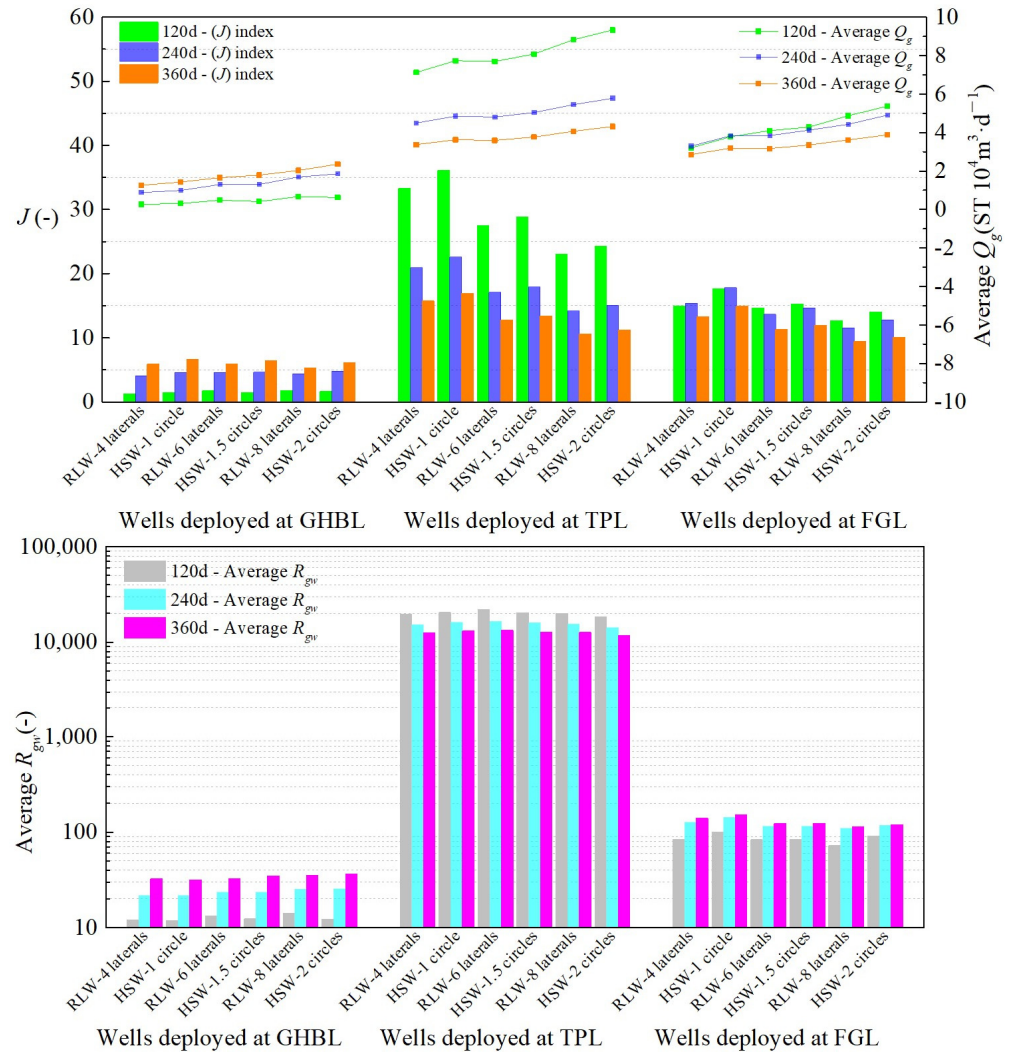
$$J = Q_g / h \Delta P \tag{3}$$

Figure 13. Histogram of average Q_g, average R_{gw} and *J* index, and t = 120, 240, 360 days.

Here, ΔP is the production pressure difference (MPa) and *h* is the well length (m). Figure 13 depicts *J* index of these well types during the 360-day production period. The productivity of these well types ranked as follows: TPL > FGL > GHBL. When these well types were deployed at the TPL, they had the best mining performance, and the HSW-1 circle well type stood out with an average Q_g of 3.63×10^4 ST m³/d and a *J*-index of 16.93. Although the average Q_g of the HSW-1 circle well type was not the highest, its *J*-index was the highest among all well types, indicating that it had the best exploitation efficiency.

3.4.2. Summary and Recommendations

Unlike traditional drilling, coiled tubing drilling has a smaller wellbore size and turning radius, providing self-propulsion through hydraulic jetting. The axial and lateral forces generated on the wellhead during radial drilling are much lower, which can greatly improve the stability of the wellhead; this method has much lower drilling and production costs, and has great potential for application in future hydrate development, which is worth further study [24]. This work was based on on-site data from China's first offshore natural gas hydrate testing and production site and numerically analyzed the production behavior

of RLW and HSW. Compared with the single vertical well production, RLW and HSW can effectively increase production capacity by enlarging the drainage area and the productivity is directly proportional to the total completion length, which is consistent with the results of many similar studies (e.g., Mahmood et al., 2021; Zhang, 2020, 2021) [25–27]. Different from the previous research results of Mahmood et al., during a short-term production period of 360 days, the overall production capacity of HSW was better than that of RLW, regardless of which layer they were deployed to [25]. This may be because previous research was based on analytical models, and factors such as the synergistic pressure reduction effect between wells could not be well considered. Meanwhile, RLW and HSW deployed at TPL had the highest production capacity during a 360-day production period. The total gas production of HSW-2 well type was about four times that of a single vertical well, reaching 1.554×10^7 ST m^3. It is worth noting that the HSW-1 circle well type stood out with an average Q$_g$ of 3.63×10^4 ST m^3/d and a J-index of 16.93; it had the highest *J*-index among all well types, which means the best mining efficiency. It is recommended to choose the HSW-1 circle well type, if the coiled tubing drilling technique is used for on-site testing production of NGHs in the future. This work still has certain limitations. In the future, it is necessary to consider the real reservoir environment to establish a three-dimensional heterogeneous model, and further combine wellbore heating or reservoir reconstruction techniques to study the production behavior of RLW and HSW in-depth.

4. Conclusions

Based on the on-site data of China's first offshore NGH testing production site in the Shenhu Sea area, an ideal interlayer heterogeneity model of the SHSC4 well was established and the productivity of RLW and HSW were numerically evaluated with different completion layers and lateral lengths. The following results were obtained:

(1) RLW and HSW can effectively improve production capacity by expanding the drainage area, which is directly proportional to the number and length of laterals and the length of the horizontal wellbore. Different from previous research results, during a short-term production period of 360 days and due to the synergistic pressure reduction effect between wellbores, the overall production capacity of HSW was better than that of RLW, regardless of which layer they were deployed to.

(2) RLW and HSW deployed at the TPL had optimal mining performance within a 360-day production period due to their highest R_{gw} performance. The V_g of the HSW-2 circles well type was about four times that of a single vertical well, reaching 1.554×10^7 ST m^3. It is worth noting that the HSW-1 circle well type stood out with an average Q_g of 3.63×10^4 ST m^3/d and a *J*-index of 16.93 after 360-day production; it had the highest *J*-index among all well types, which meant the best mining efficiency. It is recommended to choose the HSW-1 circle well type, if the coiled tubing drilling technique is used for on-site testing production of NGHs in the future.

(3) Coiled tubing drilling has a smaller wellbore size and turning radius. With the advantages of strong technical feasibility and low-cost, it has great potential for application in hydrate development. In the future, it is necessary to consider the real reservoir environment, combined with stimulation methods such as wellbore-assisted heating and reservoir reconstruction, to further investigate the gas and water production behavior of RLW and HSW in different types of NGH reservoirs.

Author Contributions: T.W.: Conceptualization, Methodology, Software, Writing—Original Draft. M.W.: Writing—review and editing, Supervision. H.L.: Resources, Funding acquisition. Z.L.: Formal analysis, Investigation. Z.C.: Formal analysis, Investigation. L.T.: Resources. Q.L.: Data curation, Visualization. J.Q.: Data curation, Visualization. J.W.: Writing-review and editing, Supervision, Project administration. All authors have read and agreed to the published version of the manuscript.

Institutional Review Board Statement: Not applicable.

Informed Consent Statement: Not applicable.

Data Availability Statement: Data will be made available on request.

Conflicts of Interest: The authors declare that they do not have any commercial or associative interest that represent conflicts of interest in connection with the submitted work.

Nomenclature

L	Open hole completion length of wellbore (m)
l	Length of each lateral wellbore (m)
n	Quantity of lateral wellbore
M^κ	Mass accumulation of component κ, (kg/m^3)
F^κ	Mass flux of component κ, $kg/(m^2 \cdot s)$
q^κ	Sink/source of component κ, $kg/(m^3 \cdot s)$
M^θ	Energy accumulation (J/m^3)
F^θ	Energy flux, $J/(m^2 \cdot s)$
q^θ	Sink/source of heat, $J/(m^3 \cdot s)$
V	Volume (m^3)
Γ	Surface area (m^2)
t	Times (s)
φ	Porosity
Q_g	Gas production rates at well (m^3/d)
Q_w	Water production rates at well (m^3/d)
V_g	Cumulative gas production at well (m^3/d)
R_{gw}	Ratio of cumulative gas to cumulative gas (ST m^3 of CH_4/m^3 of H_2O)
J	Specific production index (-)
β	Phase, $\beta = A, G, H, I$ is aqueous, gas, hydrate and ice, respectively
κ	Component, $\kappa = w, m, i, h$ is water, methane, salt, and hydrate, respectively
S_β	Saturation of phase β
T	Temperature (°C)
P_{cap}cap	Capillary pressure (Pa)
P_0	Initial capillary pressure (Pa)
S^*	Saturation for capillary pressuremodel
S_{mxA}	Maximum aqueous saturation
S_{irA}	Irreducible saturation of aqueous phase
S_{irG}	Irreducible saturation of gas phase
n_A	Permeability reduction index for aqueous phase
n_G	Permeability reduction index for gas phase
λ	Porosity distribution index
k	Permeability (m^2)
g	Gravity acceleration (m/s^2)
$k_{r\beta}$	Relative permeability of phase β

Abbreviations

OB	Overburden layer
UB	Underburden layer
GHBL	Gas hydrate bearing layer
TPL	Three phase layer
FGL	Free gas layer
NGH	Natural gas hydrate
RLW	Radial lateral well
HSW	Horizontal snake well

References

1. Sloan, E. Fundamental principles and applications of natural gas hydrates. *Nature* **2003**, *426*, 353–359. [CrossRef] [PubMed]
2. Boswell, R. Is gas hydrate energy within reach? *Science* **2009**, *325*, 957–958. [CrossRef] [PubMed]
3. Chong, Z.; Yang, S.; Babu, P.; Linga, P.; Li, X. Review of natural gas hydrates as an energy resource: Prospects and challenges. *Appl. Energy* **2016**, *162*, 1633–1652. [CrossRef]
4. Boswell, R.; Collett, T. Current perspectives on gas hydrate resources. *Energy Environ. Sci.* **2011**, *4*, 1206–1215. [CrossRef]

5. Yamamoto, K.; Terao, Y.; Fujii, T.; Ikawa, T.; Seki, M.; Matsuzawa, M.; Kanno, T. Operational Overview of the First Offshore Production Test of Methane Hydrates in the Eastern Nankai Trough. In Proceedings of the Offshore Technology Conference, Houston, TX, USA, 5–8 May 2014; OnePetro: Richardson, TX, USA, 2014.

6. Yamamoto, K.; Wang, X.; Tamaki, M.; Suzuki, K. The second offshore production of methane hydrate in the Nankai Trough and gas production behavior from a heterogeneous methane hydrate reservoir. *RSC Adv.* **2019**, *9*, 25987–26013. [CrossRef] [PubMed]

7. Li, J.; Ye, J.; Qin, X.; Qiu, H.; Wu, N.; Lu, H.; Xie, W.; Lu, J.; Peng, F.; Xu, Z.; et al. The first offshore natural gas hydrate production test in South China Sea. *China Geol.* **2018**, *1*, 5–16. [CrossRef]

8. Ye, J.; Qin, X.; Xie, W.; Lu, H.; Ma, B.; Qiu, H.; Liang, J.; Lu, J.; Kuang, Z.; Lu, C.; et al. The second natural gas hydrate production test in the South China Sea. *China Geol.* **2020**, *3*, 197–209. [CrossRef]

9. Wu, N.; Li, Y.; Wan, Y.; Sun, J.; Huang, L.; Mao, P. Prospect of marine natural gas hydrate stimulation theory and technology system. *Nat. Gas Ind. B* **2021**, *40*, 173–187. [CrossRef]

10. Ye, H.; Wu, X.; Li, D. Numerical Simulation of Natural Gas Hydrate Exploitation in Complex Structure Wells: Productivity Improvement Analysis. *Mathematics* **2021**, *9*, 2184. [CrossRef]

11. Mao, P.; Wan, Y.; Sun, J.; Li, Y.; Hu, G.; Ning, F.; Wu, N. Numerical study of gas production from fine-grained hydrate reservoirs using a multilateral horizontal well system. *Appl. Energy* **2021**, *301*, 117450. [CrossRef]

12. Xin, X.; Li, S.; Xu, T.; Yuan, Y. Numerical investigation on gas production performance in methane hydrate of multilateral well under depressurization in Krishna-Godavari basin. *Geofluids* **2021**, *2021*, 9936872. [CrossRef]

13. Ye, H.; Wu, X.; Li, D.; Jiang, Y. Numerical simulation of productivity improvement of natural gas hydrate with various well types: Influence of branch parameters. *J. Nat. Gas Sci. Eng.* **2022**, *103*, 104630. [CrossRef]

14. Hao, Y.; Yang, F.; Wang, J.; Fan, M.; Li, S.; Yang, S.; Wang, C.; Xiao, X. Dynamic analysis of exploitation of different types of multilateral wells of a hydrate reservoir in the South China sea. *Energy Fuels* **2022**, *36*, 6083–6095. [CrossRef]

15. Jin, G.; Peng, Y.; Liu, L.; Su, Z.; Liu, J.; Li, T.; Wu, D. Enhancement of gas production from low-permeability hydrate by radially branched horizontal well: Shenhu Area, South China Sea. *Energy* **2022**, *253*, 124129. [CrossRef]

16. He, J. Numerical simulation of a Class I gas hydrate reservoir depressurized by a fishbone well. *Processes* **2023**, *11*, 771. [CrossRef]

17. Cao, X.; Sun, J.; Qin, F.; Ning, F.; Mao, P.; Gu, Y.; Li, Y.; Zhang, H.; Yu, Y.; Wu, N. Numerical analysis on gas production performance by using a multilateral well system at the first offshore hydrate production test site in the Shenhu area. *Energy* **2023**, *270*, 126690. [CrossRef]

18. Cinelli, S.; Kamel, A. Novel technique to drill horizontal laterals revitalizes aging field. In Proceedings of the SPE/IADC Drilling Conference and Exhibition, Amsterdam, The Netherlands, 5–7 March 2013.

19. Kamel, A. RJD: A cost effective frackless solution for production enhancement in marginal fields. In Proceedings of the SPE Eastern Regional Meeting, Canton, OH, USA, 13–15 September 2016.

20. Kamel, A. Radial Jet Drilling: A Technical Review. In Proceedings of the SPE Middle East Oil & Gas Show and Conference, Manama, UK, 8 March 2017.

21. Kamel, A. A technical review of radial jet drilling. *J. Pet. Gas Eng.* **2017**, *8*, 79–89.

22. Huang, Z.; Huang, Z. Review of Radial Jet Drilling and the key issues to be applied in new geo-energy exploitation. *Energy Procedia* **2019**, *158*, 5969–5974. [CrossRef]

23. Wan, L.; Shaibu, R.; Hou, X.; Guo, B. A feasibility study of producing natural gas from subsea hydrates with horizontal snake wells. In Proceedings of the Offshore Technology Conference Brasil. OTC, Rio de Janeiro, Brasil, 29–31 October 2019; D011S014R006.

24. Li, G.; Tian, S.; Zhang, Y. Research progress on key technologies of natural gas hydrate exploitation by cavitation jet drilling of radial wells. *Pet. Sci. Bull.* **2020**, *5*, 349–365.

25. Mahmood, M.; Guo, B. Productivity comparison of radial lateral wells and horizontal snake wells applied to marine gas hydrate reservoir development. *Petroleum* **2021**, *7*, 407–413. [CrossRef]

26. Zhang, P.; Tian, S.; Zhang, Y.; Li, G.; Zhang, W.; Khan, W.; Ma, L. Numerical simulation of gas recovery from natural gas hydrate using multi-branch wells: A three-dimensional model. *Energy* **2020**, *220*, 119549. [CrossRef]

27. Zhang, P.; Tian, S.; Zhang, Y.; Li, G.; Wu, X.; Wang, Y. Production simulation of natural gas hydrate using radial well depressurization. *Pet. Sci. Bull.* **2021**, *3*, 417–428.

28. Zhang, P.; Zhang, Y.; Wang, W.; Wang, T.; Tian, S. Experimental study on natural gas hydrate extraction with radial well depressurization. *Pet. Sci. Bull.* **2022**, *03*, 382–393.

29. Wan, T.; Yu, M.; Lu, H.; Chen, Z.; Li, Z.; Tian, L.; Li, K.; Huang, N.; Wang, J. Numerical Simulation of Vertical Well Depressurization with Different Deployments of Radial Laterals in Class 1-Type Hydrate Reservoir. *Energies* **2024**, *17*, 1139. [CrossRef]

30. Zhang, W.; Liang, J.; Lu, J.; Wei, J.; Su, P.; Fang, Y.; Guo, Y.; Yang, S.; Zang, G. Accumulation features and mechanisms of high saturation natural gas hydrate in shenhu area, northern south china sea. *Pet. Explor. Dev.* **2017**, *44*, 708–719. [CrossRef]

31. Moridis, G.; Kowalsky, M.; Pruess, K. *TOUGH+ Hydrate V1.0 User's Manual*; Report LBNL-0149E; Lawrence Berkeley National Laboratory: Berkeley, CA, USA, 2008.

32. Zhang, K.; Moridis, G.; Wu, Y.; Pruess, K. A domain decompositionapproach for large-scale simulations of flow processes in hydrate-bearing geologic media. In Proceedings of the 6th International Conference on Gas Hydrates, ICGH 2008, Vancouver, BC, Canada, 6–10 July 2008.

33. Kowalsky, M.; Moridis, G. Comparison of kinetic and equilibrium reaction models in simulating gas hydrate behavior in porous media. *Energy Convers. Manag.* **2007**, *48*, 1850–1863. [CrossRef]

34. Sun, J.; Zhang, L.; Ning, F.; Lei, H.; Liu, T.; Hu, G.; Lu, H.; Lu, J.; Liu, C.; Jiang, G.; et al. Production potential and stability of hydrate-bearing sediments at the site GMGS3-W19 in the South China Sea: A preliminary feasibility study. *Mar. Pet. Geol.* **2017**, *86*, 447–473. [CrossRef]

35. Yuan, Y.; Xu, T.; Xin, X.; Xia, Y. Multiphase Flow Behavior of Layered Methane Hydrate Reservoir Induced by Gas Production. *Geofluids* **2017**, *2017*, 7851031. [CrossRef]

36. Sun, J.; Ning, F.; Li, S.; Zhang, K.; Liu, T.; Zhang, L.; Jiang, G.; Wu, N. Numerical simulation of gas production from hydrate-bearing sediments in the Shenhu area by depressurising: The effect of burden permeability. *J. Unconv. Oil Gas Resour.* **2015**, *12*, 23–33. [CrossRef]

37. Moridis, G.; Kowalsky, M.; Pruess, K. Depressurization-induced gas production from class 1 hydrate deposits. *SPE Reserv. Eval. Eng.* **2007**, *10*, 458–481. [CrossRef]

38. Feng, Y.; Chen, L.; Suzuki, A.; Kogawa, T.; Okajima, J.; Komiya, A.; Maruyama, S. Enhancement of gas production from methane hydrate reservoirs by the combination of hydraulic fracturing and depressurization method. *Energy Convers. Manag.* **2019**, *184*, 194–204. [CrossRef]

39. Yuan, Y.; Xu, T.; Jin, C.; Zhu, H.; Gong, Y.; Wang, F. Multiphase flow and mechanical behaviors induced by gas production from clayey-silt hydrate reservoirs using horizontal well. *J. Clean. Prod.* **2021**, *328*, 129578. [CrossRef]

40. Sun, Y.; Ma, X.; Guo, W.; Jia, R.; Li, B. Numerical simulation of the short- and long-term production behavior of the first offshore gas hydrate production test in the South China Sea. *J. Pet. Sci. Eng.* **2019**, *181*, 106196. [CrossRef]

41. Ma, X.; Sun, Y.; Liu, B.; Guo, W.; Jia, R.; Li, B.; Li, S. Numerical study of depressurization and hot water injection for gas hydrate production in China's first offshore test site. *J. Nat. Gas Sci. Eng.* **2020**, *83*, 103530. [CrossRef]

42. Yu, T.; Guan, G.; Wang, D.; Song, Y.; Abudula, A. Numerical investigation on the long-term gas production behavior at the 2017 Shenhu methane hydrate production-site. *Appl. Energy* **2021**, *285*, 116466. [CrossRef]

43. Li, S.X.; Yu, X.; Li, S. Prediction of gas production of Shenhu hydrate reservoir by depressurization and its simulation treatment. *China Offshore Oil Gas* **2020**, *32*, 122–127.

44. Qin, X.; Liang, Q.; Ye, J.; Yang, L.; Qiu, H.; Xie, W.; Liang, J.; Lu, J.; Lu, C.; Lu, H.; et al. The response of temperature and pressure of hydrate reservoirs in the first gas hydrate production test in South China Sea. *Appl. Energy* **2020**, *278*, 115649. [CrossRef]